Multifocal Ectopic Purkinje-Related Premature Contractions: A New SCN5A-Related Cardiac Channelopathy.

Gabriel Laurent, Samuel Saal, Mohamed Yassine Amarouch, Delphine M. Béziau, Roos F. J. Marsman, Laurence Faivre, Julien Barc, Christian Dina, Geraldine Bertaux, Olivier Barthez, et al.

Multifocal Ectopic Purkinje Premature Contractions: a new SCN5A-related cardiac channelopathy

Gabriel Laurent, MD, PhD, Samuel Saal, MD, Mohamed Yassine Amarouch, PhD, Delphine M Beziau, MSc, Roos FJ Marsman, MSc, Laurence Faivre, MD, PhD, Julien Barc, PhD, Christian Dina, PhD, Geraldine Bertaux, MD, Olivier Barthez, MD, Christel Thauvin-Robinet, MD, PhD, Philippe Charron, MD, PhD, Véronique Fressart, MD, PhD, Alice Maltret, MD, Elisabeth Villain, MD, Estelle Baron, BA, Jean Mérot, PhD, Rodolphe Turpault, PhD, Yves Coudière, PhD, Flavien Charpentier, PhD, Jean Jacques Schott, PhD, Gildas Loussouarn, PhD, Arthur A. M. Wilde, MD, PhD, Jean Eric Wolf, MD, PhD, Isabelle Baró, PhD, Florence Kyndt, PharmD, PhD, Vincent Probst, MD, PhD.

J. Am. Coll. Cardiol. **2012; 60:144-156.**

ONLINE DATA SUPPLEMENT

http://dx.doi.org/10.1016/j.jacc.2012.02.052

SUPPLEMENTAL METHODS

Mutation analysis

The proband (III.1) of family 1 was screened for mutations in *LMNA* encoding lamin A/C, *ABCC9* encoding SUR2A and SCN5A. All 12 coding exons and intronic junctions of *LMNA* were amplified and scanned using an HRMA/sequencing method (conditions available under request) using the Light-Cycler® 480 High Resolution Melting Master kit according to the manufacturer's instructions (Roche Applied Science, Meylan, France) and further scanned by HRM analysis. PCR products showing divergent HRM profiles were purified and directly sequenced on both strands using the BigDye® Terminator v.3.1 Cycle Sequencing Kit (Applied Biosystems, Forster City, CA). After purification, sequencing products were applied onto an ABI 3730 automatic sequencer (Applied Biosystems). Screening for mutation in *ABCC9* gene was performed as previously described (1).

Screening for mutation in *SCN5A* was performed by a polymerase chain reaction amplification of coding regions and flanking intronic sequences (primers sequences available under requests) followed by bidirectional sequencing of amplicons using the BigDye® Terminator v.3.1 Cycle Sequencing Kit (Applied Biosystems, Forster City, CA. After purification, sequencing products were applied onto on an ABI PRISM 3730 DNA sequence detection system (Applied Biosystems).

Exon 6 of *SCN5A*, which includes the c.665G>A transition, was amplified from genomic DNA of family 1 and 2 members with primers CACCCCCTTTCCTCCTCT and CCAGGCATATCCCTCTAGCC. The purified PCR product was sequenced using BigDye Terminator 3.1 (Applied Biosystems) chemistry.

For family 3, exon 6 of *SCN5A* was amplified from genomic DNA of the proband II-3 and the purified PCR product similarly sequenced. The sequence variant present in

all affected family members was further confirmed by digestion with HinfI (New England BioLabs, Beverly, MA). HinfI digests the fragment containing c.665G but does not digest that with c.665A.

Six hundred Caucasian control chromosomes from Human Random Control (HRC) panels were screened for the presence of the c.665G>A transition using HRM (High Resolution Melting) assay on the LightCycler 480 System (Roche) and the same primers.

Haplotype Analysis

To ascertain whether there is a common disease haplotype for the R222Q mutation of the *SCN5A* gene in the two families with MEPT, and estimate the low limit of the most recent common ancestor, 10 microsatellite markers around the *SCN5A* gene (D3S1759, D3S2432, D3S3047, D3S3512, D3S1298, intragenic *SCN5A* marker, D3S3521, D3S3527, D3S3522 and D3S3559) were genotyped in individuals from the 3 families. Haplotype analysis was performed in 12 members of family 1 (9 affected), 3 members of family 2 (2 affected) and 3 members of family 3 (3 affected).

The primer sequences were obtained from Ensembl (www.ensembl.org) except for the intragenic marker. Each marker was amplified by PCR and the sense primers were 5'-end labeled with fluorescence (R6G and R110-dCTP, Perkin Elmer).

PCR was performed under the following conditions: denaturation at 94°C for 3 min; 30 cycles of denaturation at 94°C for 30 sec, annealing at 55°C for 30 sec, and extension at 72°C for 1 min; final extension at 72°C for 10 min. Alleles were submitted to electrophoresis using an ABI PRISM 3730 DNA analyser, (PE Applied Biosystems), with ROX-500 size standard (PE Applied Biosystems). Genotype analysis was automated using GeneMapper software, version 4.0 (PE Applied Biosystems).

We estimated the age of the mutation using the Genin and collaborators method (2), based on the length of identity by state segments around the mutation. This method identifies the closest markers at which the two affected individuals do not share any allele on either side. The likelihood is built on the number of recombination events between the mutation and the neighboring genetic markers, with a correction through the possibility of mutation. Because we did not have even a single common allele in the haplotypic background of families 1 and 2, we created two dummy markers, with shared common allele by both affected individuals at a recombination fraction θ=0.0001 both upstream and downstream the mutation. Thus, we were aiming at finding a lower threshold to the number of generations to the most recent common ancestor. We adopted a micro-satellite mutation rate of $m=3.10^{-3}$ (using the Stepwise Mutation Model), as proposed in the literature (3). It is noteworthy that the time to the Most Recent Common Ancestor is not necessarily the time to the mutation occurrence. Therefore, our number of generations is also a lower bound for the age of the allele.

Site-directed mutagenesis

Site-directed mutagenesis was performed on pCI-SCN5A (4) using the Quick-Change site-directed mutagenesis kit (Stratagene) according to the manufacturer's instructions. The construct was completely sequenced to ensure that there was no other mutation.

Cellular electrophysiology

The African green monkey kidney fibroblast-like cell line (COS-7) was obtained from the American Type Culture Collection and cultured as previously described (5). Cells were transfected with DNA complexed to JetPEI (Polyplus-tranfection) according to

the manufacturer's instructions. Relative DNA concentrations were 10% pCI-Nav1.5 (RefSeq NG_008934.1) WT or R222Q, or 5% of each for the heterozygous condition), 10% pRC-hβ1 (4) and 80% pEGFP (Clontech). The resulting Nav1.5 protein is the splice variant containing H 558 and Q1077 amino acids. At eight hours post-transfection, the cells were isolated and seeded in plastic Petri dishes at low density. At twenty-four hours post-transfection, whole-cell currents were recorded at room temperature using the patch-clamp technique. The cells were continuously superfused with Tyrode solution containing (in mmol/L): NaCl 145, KCl 4, $MgCl_2$ 1, $CaCl_2$ 1, HEPES 5, glucose 5, pH adjusted to 7.4 with NaOH. Wax-coated pipettes (tip resistance: 1.8 to 3 MΩ) were filled with intracellular medium containing (in mmol/L): NaCl 10, CsCl 64.5, aspartic acid 70.5, HEPES 5, pH adjusted to 7.2 with CsOH. During data recording, the studied cell was locally superfused with extracellular medium containing (in mmol/L): NaCl 145, CsCl 4, $CaCl_2$ 1, $MgCl_2$ 1, HEPES 5, glucose 5, pH adjusted to 7.4 with NaOH with 30 µM quinidine or 30 µM tetrodotoxin (TTX) when needed. All products were purchased from Sigma, except TTX, provided by Tocris Bioscience. Stimulation, data recording through an A/D converter (Tecmar TM100 Labmaster, Scientific Solutions; 5 kHz filtering), and analysis were performed with Acquis1 software (Bio-Logic). All current measurements were normalized using the cell capacitance. Capacitance and series resistances were compensated (60-70% compensation) to obtain minimal contribution of capacitive transients using an Axopatch 200A amplifier (Axon Instruments, Inc).

Mathematical modeling of ventricular and Purkinje action potentials

Single-cell models

The same strategy was used for both models of the human Purkinje cells (6) and left-ventricular myocytes (7). The left-ventricular myocytes model was modified from the CellML.org model (April 27, 2010) in order to minimize the stimulation artifact (stimulation amplitude: -50 µA/µF; stimulation duration: 0.5 ms; GNa 100 ms/µF). The equations corresponding to the Na^+ current were iteratively modified to reproduce the relative variation of 8 parameters due to the R222Q mutation (i.e. peak amplitude at -20 mV, half-activation potential, activation slope, time to peak at -20 mV, half-inactivation potential, inactivation slope and the kinetics of inactivation at -35 mV and recovery from inactivation at -100 mV). The other currents generating the action potential were not modified.

In the Purkinje cell model, the effects of the R222Q mutation were simulated by (i) modifying α_m and β_m to recapitulate the shift in the activation curve and (ii) modifying β_h to recapitulate the shift in the inactivation with no change in the recovery from inactivation. The WT and R222Q Na^+ current formulations followed the DiFrancesco and Noble model (6) as such:

WT	**R222Q**
α_h = 20 x exp(-0.125 x (V + 75))	α_h = 20 x exp(-0.125*(V + 75))
β_h = 2000/(320 x exp(-0.1x (V + 75))+1)	β_h = 2000/(320 x exp(-0.1 x (V + 75 + **10**))+1)
α_m = 200 x (V+ 41)/(1-exp(-0.1 x (V + 41)))	α_m = 200 x (V+ 41+**shift**)/(1-exp(-0.1 x (V + 41 + **shift**)))
β_m = 8000 x exp(-0.056 x (V + 66))	β_m = 8000 x exp(-0.056 x (V + 66 + **shift**))

where “shift” was set to 12 to best fit the shift in the activation curve. This value was also used in the multicellular model. But interestingly, in the unicellular model, an excessive Na^+ window current prevented repolarization and the value had to be decreased to 9 to observe an action potential.

To mimic the heterozygous condition, the Na^+ current resulted from the summation of half the WT current and half the R222Q current.

In the ventricular cell model, the effects of the R222Q mutation were simulated (i) by modifying all the forward transitions ($\alpha,\beta,\gamma,\gamma\gamma,\eta$) to recapitulate the shift in the activation curve and (ii) by decreasing the inactivation/activation coupling factor to recapitulate the smaller shift in the inactivation curve with no change in the recovery from inactivation kinetics. The WT and R222Q Na^+ current formulation followed model (7) as such:

WT	**R222Q**
α = 26 x exp(0.011 x V)	η = 26 x exp(0.011 x (V**+11**))
β = 0.036 x exp(-0.090 x V)	β = 0.036 x exp(-0.090 x (V**+11**))
γ = 590 x exp(0.110 x V)	γ = 590 x exp(0.110 x (V**+11**))
$\gamma\gamma$ = 2.6 x exp(0.030 x V)	$\gamma\gamma$ = 2.6 x exp(0.030 x (V**+11**))
η = 26 x exp(0.084 x V)	η = 26 x exp(0.084 x (V**+11**))
a = 1.4004	a = **1.21**

The other transition constants were not changed.

Both the Purkinje and ventricular Na^+ currents were modeled with Model Maker v4.0 (AP Benson, Wallingford, UK) and with a home-made program running on C++. The action potentials (APs) were modeled with a home-made program running on C++.

Multicellular model

Both models of the human left-ventricular subepicardial myocytes and Purkinje cells were incorporated in a multicellular model. In this model, the propagation of the electrical waves in the cardiac tissues was described by a monodomain model (8).

The membrane potential is described by a variable V following the partial differential equation:

$$A_m C_m \frac{\partial V}{\partial t} - \nabla.(D\nabla V) = A_m I_{ion}$$

Where t is the time in s, V is the transmembrane potential in mV, Am is the ratio of membrane surface per cell volume unit [1e3 cm^{-1}], Cm is the membrane capacitance per surface unit [1e-3 $mF.cm^{-2}$], and D is the average electrical conductivity of the tissue [20 $mS.cm^{-1}$ in Purkinje cells, and 1.3 $mS.cm^{-1}$ in ventricular cells]. The ionic current per surface unit I_{ion} [$\mu A.cm^{-2}$] was computed according to the models introduced above. The values of D were adjusted to obtain a propagation speed in the range of around 180 cm/s in the Purkinje system, and 90 cm/s in the ventricle. The numerical simulations were performed on a simplified 2D slice model described previously (9). The pacing site was located at the proximal part of the Purkinje fiber (see Figure. 5). The ordinary differential equations of the ionic model were integrated by a mixed explicit-implicit method, with a 1-µs step. To mimic the quinidine effects, I_{Na}, I_{to} and I_{Kr} were reduced based on the results of Wu (10;11;12) for I_{Na} and I_{Kr}, and Wang (13) for I_{to}. For the first test, we chose 10 µM quinidine, the maximal therapeutic dose *i.e.* preserving 50% I_{Na}, 30% I_{Kr} (12) and 30% I_{to} (13). Assuming that the mimicked doses were in the linear zone of the concentration-dose relationship for inhibition of the different ion currents, we also computed the consequences of preserving 75% I_{Na} and 45% I_{Kr} and I_{to} and of 85% and 50%, respectively. The computations were performed on a mesh with 2225 vertices using the cluster from the *Centre de Calcul Intensif des Pays de Loire*.

SUPPLEMENTAL RESULTS

Haplotype analysis

The alleles of 4 SCN5A flanking markers (D3S3512, D3S1298, D3S3521, D3S3527) and of the intragenic SCN5A marker were shared by the affected individuals in each family, but differed between the families 1 and 2, and 2 and 3. These results indicate that the cosegregating haplotype was different in each of these families, suggesting independent mutations origin. Using the method of Genin and collaborators, we found at least 126 generations from a hypothetical most recent common ancestor (95% confidence interval from 37 to 464 generations) for families 1 and 2. Such an ancient common origin does not fit with the fact that the observed mutation allele frequency is below 9.10^{-3} (higher bound confidence interval for no observation in 300 control individuals). The probands of families 1 and 3 shared at least two frequent microsatellite alleles (D3S1298 and D3S3512) but not the rare intragenic one. As a conclusion, families 1 and 3 may be at least 28-generation distantly related.

Computer modeling shows that ventricular cells better tolerate the mutation than Purkinje cells.

To get insights on the R222Q mutation effect on the action potentials (APs) at a cellular scale, we carried out computer simulations to evaluate the impact of the mutation on the Na^+ current in unicellular models of Purkinje and ventricular cells (6-7). The models modifications operated to mimic the mutation-induced changes in the Na^+ current have been detailed in the Supplemental Methods section. The relative shift in activation and inactivation curves in the heterozygous state, as well as all other changes of the biophysical parameters were compared to those experimentally measured in heterozygous state. Despite that the transfected cell population may be

a mixture of cells expressing mainly WT, R222Q or both Nav1.5 channels, the experimental ‘heterozygous’ parameters were successfully reproduced in both the Purkinje (Supplemental Figure 5B) and ventricular (Supplemental Figure 5C) cell models. Interestingly, when the equations mimicking the heterozygous state of the patients were introduced into the ventricular cell model, minor changes in AP morphology were observed (Supplemental Figure 6). Conversely, when the equations mimicking the heterozygous state were introduced in the Purkinje cell model, the effect was drastic: AP could not be induced (not shown). AP could be generated only if the shift in the activation curve was reduced (4 instead of 6 mV), in order to limit the Na^+ current increase (Supplemental Figure 6). But AP morphology was still highly affected. This disappeared at higher pacing rates, consistent with PVCs disappearing during exercise (Supplemental Figure 6).

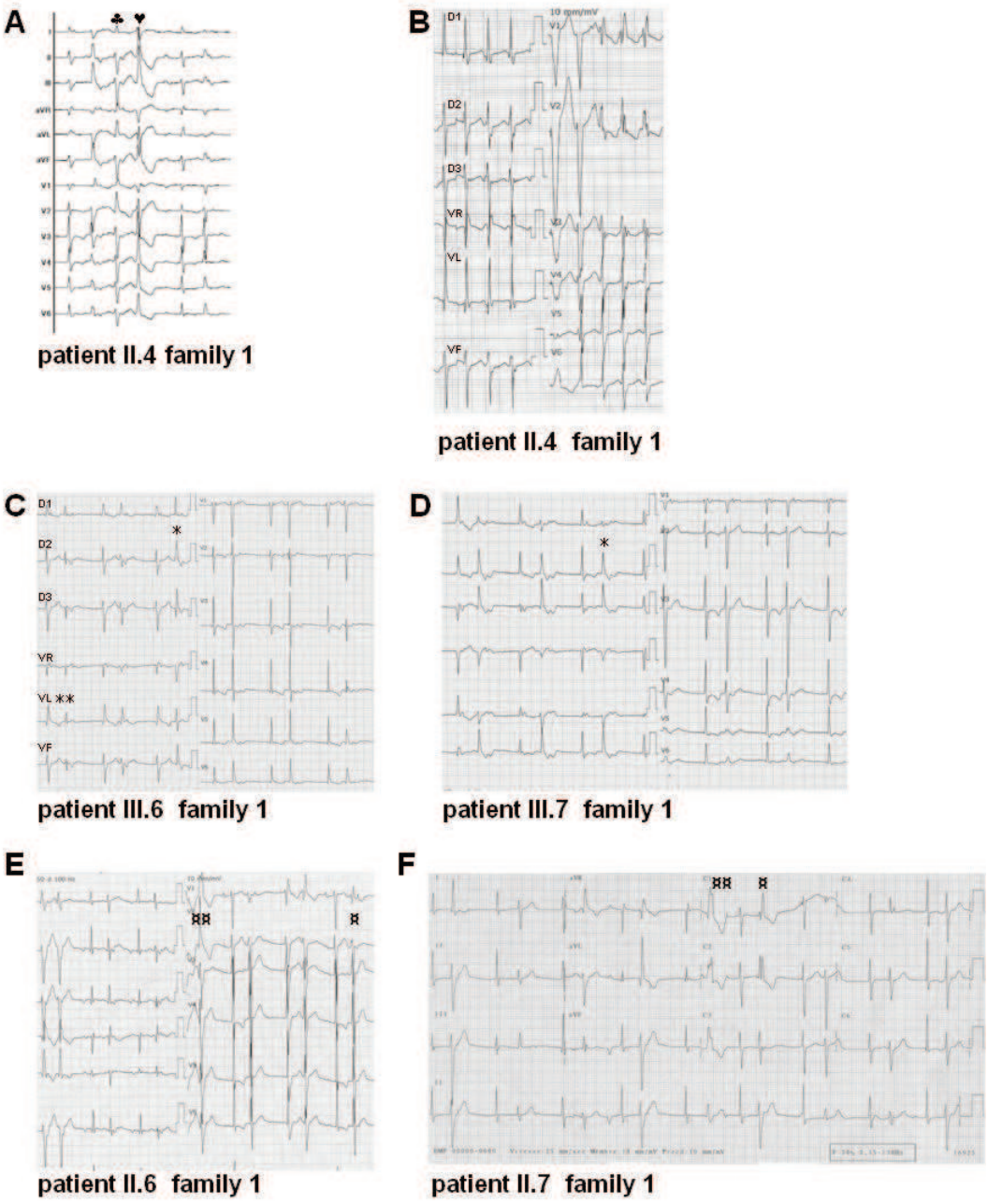

Supplemental Figure 1. Representative ECGs of family 1. Some patients (**A**) had PVC with RBBB patterns and alternant extreme variations in the axis from right (♣) to left (♥), from beat to beat. Recurrent monomorphic non-sustained ventricular tachyarrhythmia (NSVT) (**B**), and slightly polymorphic NSVT were also observed. In some patients, PVCs were relatively narrow QRS complexes (**C-D**), very similar to either sinus or junctional complexes with slight variations in the left axis from +60° (*) to -30° (**). In some patients (**E-F**), PVCs had RBBB patterns with various widths from relatively narrow (¤) to wide QRS complexes (¤¤).

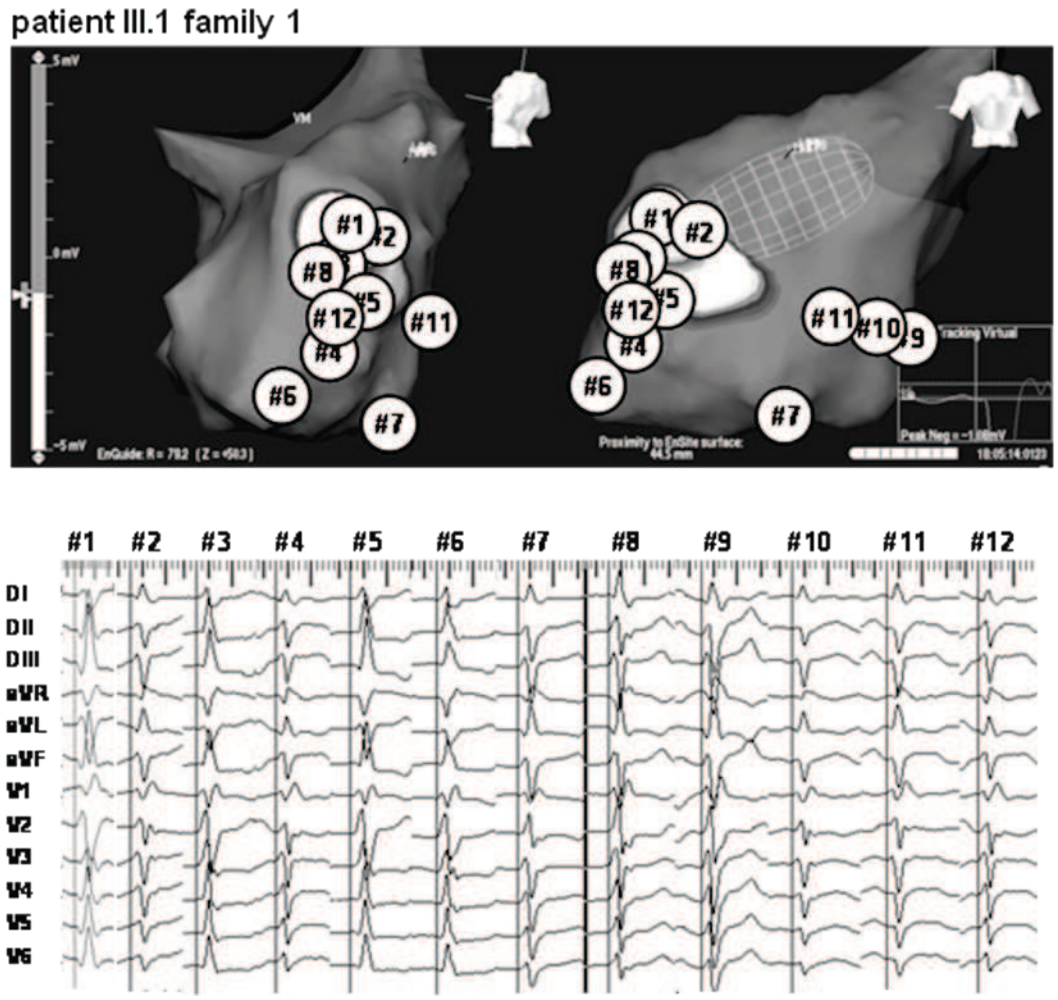

Supplemental Figure 2. Endocardial electroanatomic mapping of the left ventricle. Activation mapping of 12 different PVCs in patient III.1 (family 1). A Multi-array balloon (NavX system) helped us to pinpoint the precise location of ectopic foci along the anterior and posterior regions of the left ventricle corresponding to the extension of the left anterior and posterior fascicles.

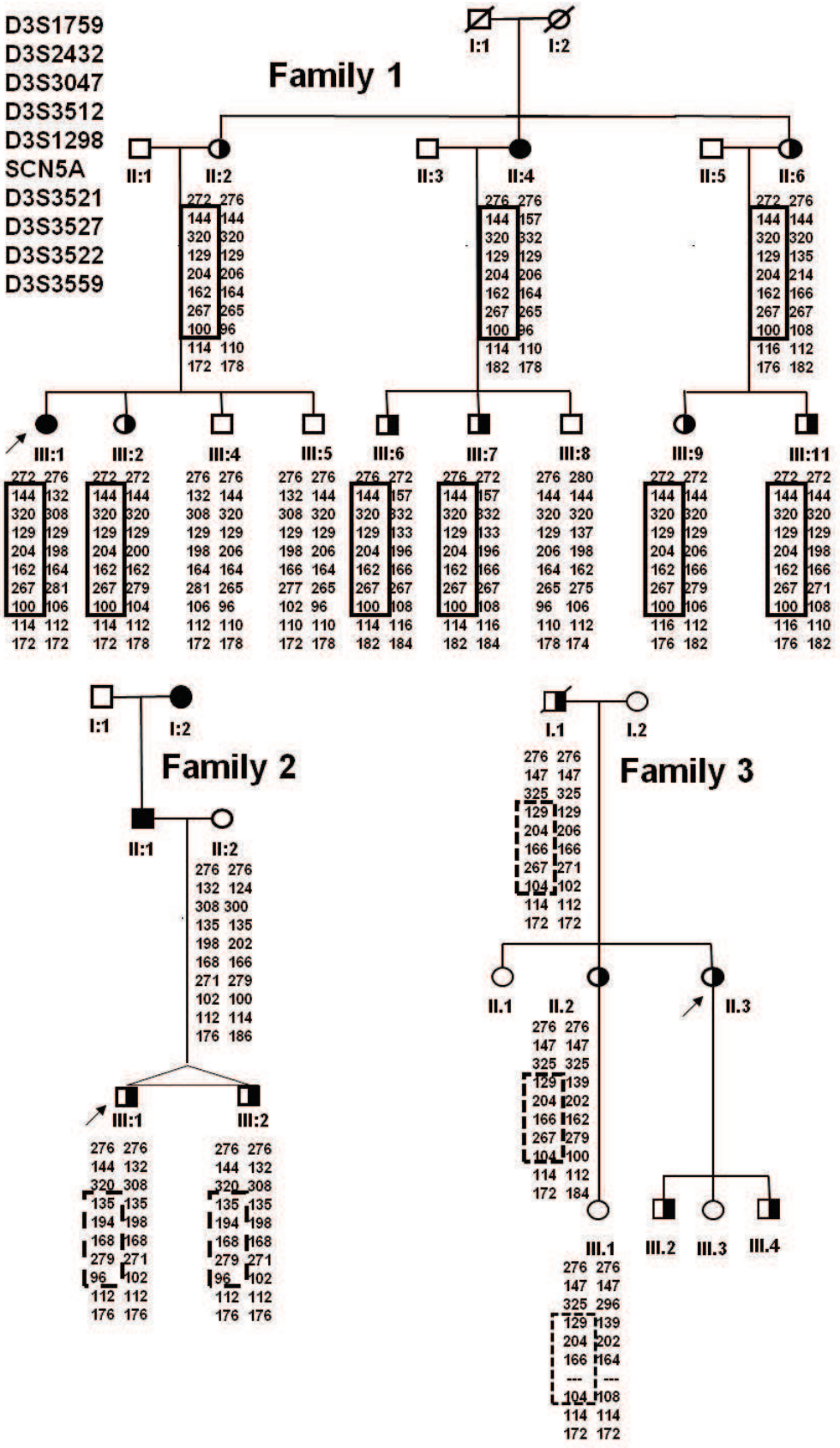

Supplemental Figure 3. Haplotype analysis of chromosome 3 in selected members for families 1, 2 and 3. Females are represented by circles and males are

represented by squares. Members affected with arrhythmia are indicated with a half-filled symbol. Members affected with arrhythmia and dilated cardiomyopathy (DCM) are indicated in black. Ten microsatellite markers (D3S1759, D3S2432, D3S3047, D3S3512, D3S1298, intragenic *SCN5A* marker, D3S3521, D3S3527, D3S3522 and D3S3559) spanning the region of chromosome 3 where the *SCN5A* gene lies, were analyzed. The disease-associated haplotype is indicated by a black frame. The disease haplotype in family 2 differed from that in family 1, showing that the R222Q mutation has arisen independently in these two families. Common alleles of two microsatellites are shared by families 1 and 3 implying a possible most recent common ancestor at least 28 generations earlier.

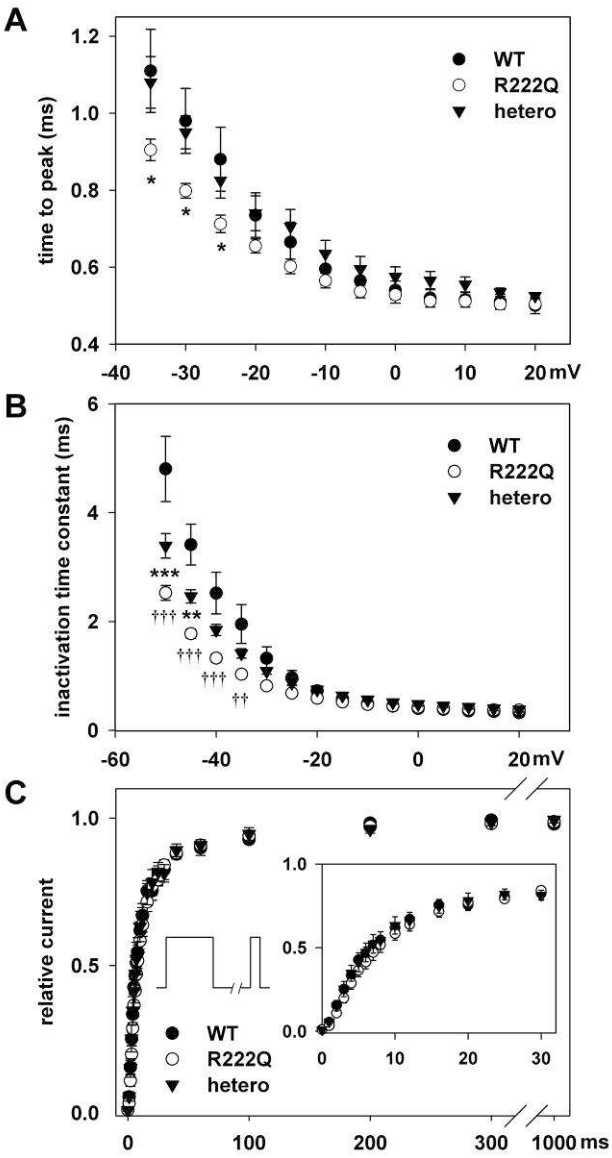

Supplemental Figure 4. Experimental effects of R222Q mutation on Nav1.5 channel in COS-7 cells. (**A**) Na^+ current time-to-peak values were used to evaluate the activation kinetics. Same transfection and voltage protocol as in Figure 4A. Tukey test: *, p<0.05 *vs* WT. (**B**) Accelerated inactivation in the presence of the R222Q mutation. Inactivation time constants were measured by fitting the inactivation phase of the Na^+ current to a single exponential equation. Tukey test: Heterozygous *vs.* WT, **: p<0.01, ***: p <0.001; R222Q *vs* WT, †: p<0.05, †††: p<0.001. (**C**) Recovery from inactivation was measured using a twin-pulse protocol (left inset: holding potential: –100 mV, 100-ms depolarization to -20 mV, back to -100 mV for 0 to 1000-ms delay before test pulse to -20 mV, frequency:0.1 Hz). Right inset: same as main graph for short delays.

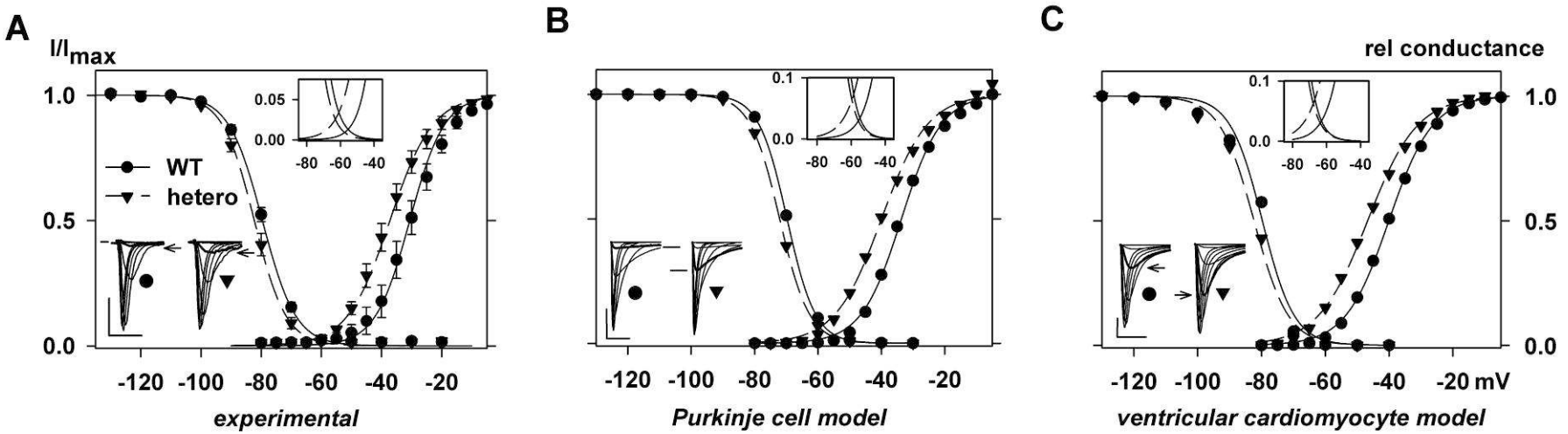

Supplemental Figure 5. (**A**) Superimposed activation and inactivation curves of WT (circles, solid line) and heterozygous (triangles, dashed line) channels obtained experimentally. Bottom inset: superimposed Na^+ current recordings using the same voltage protocol as in figure 4. Scale bars: 2 ms, 1000 pA. Top inset: increase of the predicted voltage window current in the presence of the mutation. (**B**) and (**C**) Simulated curves of WT (circles, solid line) and heterozygous (triangles, dashed line) channels; activation and inactivation in Purkinje cell (B) and (C) ventricular cardiomyocyte models. Bottom insets, simulated Na^+ currents as in A. Scale bars: 1 ms, 100 pA (B) and 5 ms, 100 pA (C). Top insets, as in A.

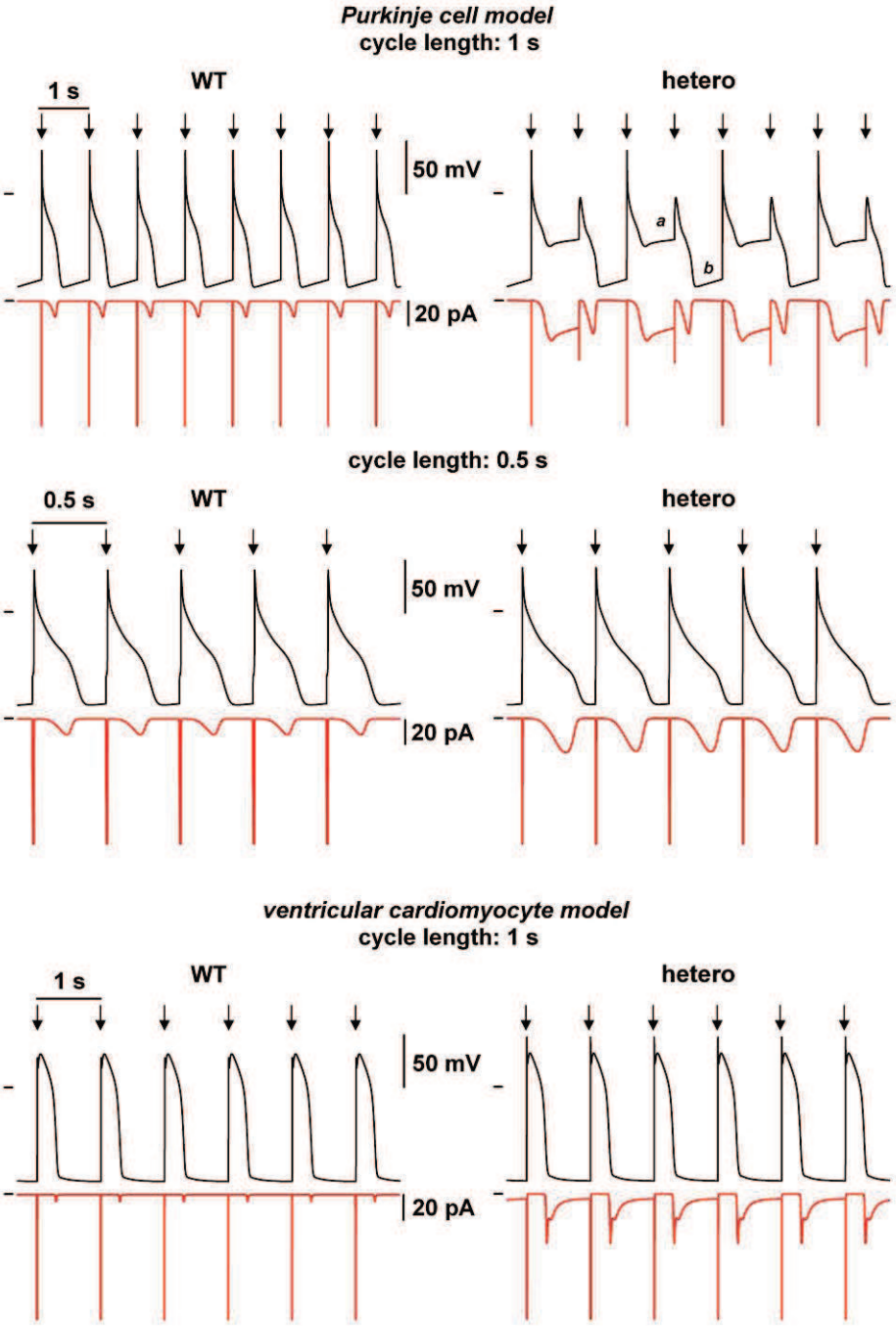

Supplemental Figure 6. Effects of the R222Q mutation on Purkinje (top) and ventricular (bottom) cell action potentials (APs) and Na^+ current obtained in the single-cell model. Simulated AP (black) and late Na^+ current (red) in WT (left) and heterozygous (right) conditions at the indicated cycle lengths. Arrows: external stimulus.

Supplemental movies

Simulation of the AP propagation from a Purkinje fiber to ventricular tissue (dimensions and stimulation shown in Figure 4), in WT (a) and heterozygous (b) conditions at cycle length of 1 s (A) and 0.5 s (B).

Supplemental Table 1: Effects of R222Q mutation on Nav1.5 biophysical parameters.

	current density	activation		inactivation		recovery from inactivation	window current		
	peak at –20 mV (pA/pF)	$V_{1/2}$ (mV)	k (mV)	$V_{1/2}$ (mV)	k (mV)	$t_{1/2}$ (ms)	g_{max} (pS/pF)	E_{max} (mV)	AUC (a.u.)
WT	–205.8±29.3 (36)	–30.6±2.1 (9)	5.7±0.3 (9)	–79.6±0.7 (10)	5.6±0.2 (10)	7.6±0.6 (6)	15.9±2.6 (13)	-42.8±0.5 (12)	29.9±3.9 (13)
heterozygous	–196.5±17.6 (48)	–37.2±1.6* (9)	7.1±0.3** (9)	–82.2±1* (9)	5.3±0.1 (9)	7.9±1.1 (8)	-	-	-
R222Q	–250.4±24.8 (44)	–42.3±1.0*** (11)	6.5±0.4 (11)	–84.6±0.7*** (8)	4.8±0.2** (8)	8.8±0.9 (8)	19.1±2.0 (14)	-58.6±1.1*** (14)	55.2±7.6** (14)

(n): number of cells; *: p<0.05; **: p<0.01; ***: p<0.001 *vs.* WT; $V_{1/2}$ and k; voltage for half-activation or -inactivation of the Na^+ current and slope; $t_{1/2}$: time to reach 50% recovery of the Na^+ current; g_{max}: maximal TTX-sensitive conductance recorded during a depolarizing-voltage ramp as in Supplemental Figure 4; E_{max}: potential at which the maximum conductance was measured. AUC: area under curve calculated on current density/membrane potential relationship; a.u.: arbitrary unit.

Supplemental Table 2: Effects of quinidine on WT and R222Q Nav1.5 currents.

		current density	window current
		peak at –20 mV (pA/pF)	**I_{max} (pA/pF)**
WT	**control**	–136.0±28.5 (12)	–1.87±0.42 (7)
	30 µM quinidine	–76.7±15.2***	–0.74±0.16*
R222Q	**control**	–123.3±20.1 (10)	–2.54±0.41 (6)
	30 µM quinidine	–63.9±10.5***	–1.17±0.12**

(n): number of cells; paired t-test: *: p<0.05; **: p<0.01; ***: p<0.001 *vs.* control; window current: TTX-sensitive (30 µM) current elicited by a depolarizing-voltage ramp; I_{max}: current density measured when the TTX-sensitive conductance is maximal (*i.e.* at -43 mV and -59 mV for WT and R222Q, respectively).

SUPPLEMENTAL REFERENCES

1 Bienengraeber M, Olson TM, Selivanov VA, Kathmann EC, O'Cochlain F, Gao F, Karger AB, Ballew JD, Hodgson DM, Zingman LV, Pang YP, Alekseev AE, Terzic A. ABCC9 mutations identified in human dilated cardiomyopathy disrupt catalytic KATP channel gating. Nat Genet. 2004;36:382-387.

2 Genin E, Tullio-Pelet A, Begeot F et al. Estimating the age of rare disease mutations: the example of Triple-A syndrome. J Med Genet 2004;41:445-449.

3 Brinkmann B, Klintschar M, Neuhuber F et al. Mutation rate in human microsatellites: influence of the structure and length of the tandem repeat. Am J Hum Genet 1998;62:1408-1415.

4 Kyndt F, Probst V, Potet F et al. Novel SCN5A mutation leading either to isolated cardiac conduction defect or Brugada syndrome in a large French family. Circulation 2001;104:3081-3086.

5 Loussouarn G, Park KH, Bellocq C et al. Phosphatidylinositol-4,5-bisphosphate, PIP2, controls KCNQ1/KCNE1 voltage-gated potassium channels: a functional homology between voltage-gated and inward rectifier K+ channels. EMBO J 2003;22:5412-5421.

6 DiFrancesco D, Noble D. A model of cardiac electrical activity incorporating ionic pumps and concentration changes. Philos Trans R Soc Lond B Biol Sci 1985;307:353-398.

7 Iyer V, Mazhari R, Winslow RL. A computational model of the human left-ventricular epicardial myocyte. Biophys J 2004;87:1507-1525.

8 Keener J, Sneyd J. Mathematical Physiology , 2nd edition. Springer, 2001.

9 Aslanidi OV, Stewart P, Boyett MR et al. Optimal velocity and safety of discontinuous conduction through the heterogeneous Purkinje-ventricular junction. Biophys J 2009;97:20-39.

10 Roden DM, Bennett PB, Snyders DJ et al. Quinidine delays IK activation in guinea pig ventricular myocytes. Circ Res 1988;62:1055-1058.

11 Sanchez-Chapula JA, Ferrer T, Navarro-Polanco RA et al. Voltage-dependent profile of human ether-a-go-go-related gene channel block is influenced by a

single residue in the S6 transmembrane domain. Mol Pharmacol 2003;63:1051-1058.

12 Wu L, Guo D, Li H et al. Role of late sodium current in modulating the proarrhythmic and antiarrhythmic effects of quinidine. Heart Rhythm 2008;5:1726-1734.

13 Wang Z, Fermini B, Nattel S. Effects of flecainide, quinidine, and 4-aminopyridine on transient outward and ultrarapid delayed rectifier currents in human atrial myocytes. J Pharmacol Exp Ther 1995;272:184-196.